Divergent erythroid megakaryocyte fates in *Blvrb*-deficient mice establish non-overlapping cytoprotective functions during stress hematopoiesis

Natasha M. Nesbitt[a], **Lisa E. Malone**[a], **Zhaoyan Liu**[b], **Alexander Jares**[c], **Dmitri V. Gnatenko**[a], **Yupo Ma**[c], **Wei Zhu**[b], **Wadie F. Bahou**[a,*]

[a]Department of Medicine, Stony Brook University, Stony Brook, NY, 11794, USA

[b]Department of Applied Mathematics and Statistics, Stony Brook University, Stony Brook, NY, 11727, USA

[c]Department of Pathology, Stony Brook University, Stony Brook, NY, 11794, USA

Abstract

Cytoprotective mechanisms of heme oxygenases function by derivatizing heme to generate carbon monoxide, ferrous iron, and isomeric biliverdins, followed by rapid NAD(P)H-dependent biliverdin reduction to the antioxidant bilirubin using two non-overlapping biliverdin reductases that display biliverdin isomer-restricted redox activity. Although cytoprotective functions of heme oxygenases are widely recognized, concomitant effects of downstream biliverdin reductases remain incomplete. A computational model predicated on murine hematopoietic single-cell transcriptomic data identified *Blvrb* as a biological driver linked to the tumor necrosis factor stress pathway as a predominant source of variation defining hematopoietic cell heterogeneity. *In vivo* studies using *Blvrb*-deficient mice established the dispensable role of Blvrb in steady-state hematopoiesis, although model validation using aged *Blvrb*-deficient mice established an important cytoprotective function in stress hematopoiesis with dichotomous megakaryocyte-biased hematopoietic recovery. Defective stress erythropoiesis was evident in $Blvrb^{-/-}$ spleens and in bone marrow erythroid development, occurring in conjunction with defective lipid peroxidation as a marker of oxidant mishandling. Cell autonomous effects on megakaryocyte lineage bias were documented using multipotential progenitor assays. These data provide the first physiological function of murine Blvrb in a non-redundant pathway of stress cytoprotection. Divergent effects on erythroid/megakaryocyte lineage speciation impute a novel redox-regulated mechanism for lineage partitioning.

Keywords

Biliverdin reductase; Cytoprotection; Erythropoiesis; Hematopoiesis; Heme oxygenase; Megakaryocytopoiesis; Redox; Stress

1. Introduction

Cellular antioxidant handling is a critical determinant of hematopoietic lineage development [1], linking bioenergetics and reactive oxygen species (ROS) to trifurcating cellular fates affecting self-renewal, apoptosis, or differentiation. Hematopoietic stem cells (HSCs) maintain a balance between metabolically quiescent (ROS^{low}), non-cycling cells in the hypoxic bone marrow niche, with a switch to aerobic and metabolically active (ROS^{high}) phenotype associated with lineage commitment; ROS accumulation exceeding cellular oxidant handling leads to apoptotic cell death. Adaptive mechanisms for cellular antioxidant handling are differentially and temporally regulated during lineage speciation, and cumulative evidence suggests that lineage bias is controlled by metabolic substrate(s) [2], chronological age [3], or spatial localization within the bone marrow niche [4]. While the general characteristics of hierarchical lineage development continue to be refined [5], stress-based hematopoietic responses remain distinct from those in steady-state [6], although gene-delimited effects causally implicated in lineage fate remain largely uncharacterized.

Heme synthesis and catabolism are contextually placed at the interface of bioenergetics and cellular antioxidant handling, converging in a linear pathway that utilizes tricarboxylic acid (TCA) cycle-derived carbon in cataplerotic reactions of tetrapyrrole biosynthesis [7,8], linked to the cytoprotective heme degradation pathway critical to mitigating against cellular stress. Cellular accumulation of pro-oxidant free heme is minimized by heme oxygenases (HMOX1 and HMOX2) in a catabolic process that generates carbon monoxide, free ferrous iron (Fe^{2+}), and isomeric biliverdins (BV) [9–11]. Two non-redundant NAD (P)H-dependent biliverdin reductases (IXα, BLVRA and IXβ, BLVRB) lead to isomeric bilirubin (BR) generation and cellular antioxidant functions [12,13]. BLVRA retains specificity for the predominant BV IXα in adults [14], while BLVRB is promiscuous, catalyzing the reduction of non-IXα BVs [14–17], several flavins [18], and pyrroloquinoline quinones (PQQ) [19]. Erythrocytes express BLVRB as a non-physiological methemoglobin (metHb) reductase [18], although it functions as the target redox coupler in cytochrome *b*5 reductase (*CYB5R*)-deficient patients receiving methylene blue for methemoglobinemia. BLVRB physiological function(s) remain enigmatic [14,20], although recent evidence in humans implicate redox-defective BLVRB function in a physiologically-relevant thrombopoietic mechanism of hematopoietic lineage fate [21].

In this manuscript, we have applied computational and confirmatory *in vivo* studies to predict and validate murine Blvrb in a cytoprotective mechanism of hematopoietic stress, with divergent effects on erythroid/megakaryocyte (E/Meg) speciation. Stress-associated defects in aged *Blvrb*$^{-/-}$ mice are restricted to the hematopoietic compartment, and establish a requisite and non-redundant Blvrb function distinct from the predominant Hmox/Blvra pathway. Defective erythroid cytoprotection associated with disordered lipid peroxidation

occurs in conjunction with megakaryocyte-biased lineage speciation [22], suggesting a mechanism for erythrocyte/megakaryocyte partitioning during stress progenitor fate [23]. Stress-induced $Blvrb^{-/-}$ mice phenocopy the age-dependent hematopoietic abnormalities (anemia with or without thrombocytosis) previously described in human [24] and $Hmox1^{-/-}$ mice [25]. These data highlight the critical role of the heme degradation pathway downstream of Hmox in stress cytoprotection, and define a physiologically relevant function for Blvrb in regulating lineage-restricted stress hematopoiesis.

2.   Results

Mathematical modeling of hematopoietic lineage speciation.

We extracted single-cell bone marrow transcriptomic data from a murine model of steady-state hematopoiesis [26], and applied a sparse factor analytical model to identify genetic drivers underpinning sources of variation regulating hematopoietic cell heterogeneity [27]. Model integration using core molecular pathways derived from MSigDB [28] identified previously annotated TNF-α (tumor necrosis factor) and ROS pathways as primary (top two) sources of cellular variation across the entire data sets. Unexpectedly, these pathways demonstrated higher weights than cell cycle regulatory pathways (i.e. G2M checkpoint and E2F targets) (Fig. 1A). We validated these results using performance comparisons to distinguish hematopoietic stem progenitor cells (HSPCs, Lin⁻c-Kit⁺Sca1⁺), long-term hematopoietic stem cells (LT-HSCs, Lin⁻c-Kit⁺Sca1⁺CD34⁻Flk 2⁻), and multipotential progenitor cells (MPP, Lin⁻Sca1⁻c-Kit⁺ [L⁻S⁻K⁺]). Spatial reconstruction using these two pathways (comprised of a limited gene subset, N = 268) resulted in reproducible cellular stratification compared with UMAP dimension reduction plots using the broader aggregated subset of highly variable genes (Fig. 1B). While both ROS [1] and TNF-α [29] have been implicated in steady-state and stress-regulated pathways of HSC survival and progenitor fate, refined pathway annotation inherent within the model identified additional driver genes as modifiers of cellular heterogeneity (Fig. 1C). Indeed, the majority of newly added genes carried greater predictive weight than those within annotated pathways, most notable for the TNF-α pathway. Heat maps showing expression levels of the refined gene subsets confirmed cluster segregation by hematopoietic phenotype (Fig. 1D). Expression differences were most evident in the TNF-α pathway, presumably due to low-level expression of ROS pathway genes during basal hematopoiesis. Unexpectedly, *Blvrb* was identified as a progenitor-enriched genetic driver associated with stress (TNF-α) hematopoiesis.

Blvrb is predicted to partition progenitor lineages.

To better define relationships among multipotential progenitors and heme degradation (Fig. 2A), we applied a graph-based clustering algorithm that segregated cells into nine distinct genetic clusters [expanded from previously-identified four clusters [26]] (Fig. 2B). Marker gene and GSEA (gene set enrichment analysis) annotations [30] defined discrete progenitor clusters as lymphoid (*Cluster 1*: genes *Igkc*, *Ighm*, *Jchain*), myeloid (*Cluster 2*: genes *Mpo*, *Elane*, *Ctsg*), megakaryocyte (*Cluster 4*: genes *Pf4*, *Itga2b*, *F2r*), and three distinct erythroid clusters representing genetically-progressive stages of erythroid development (*Clusters* 7–9; Fig. 2C). HSPCs and LT-HSCs were encompassed within the remaining clusters 3, 5, and 6. Within the heme degradation pathway genes, only *Blvrb* was identified as a cluster-enriched

gene, demonstrating induction during terminal erythroid development and enrichment in megakaryocytes (Fig. 2D and E). Differential expression studies among progenitor clusters revealed unique *Blvrb* lineage patterns (Fig. 2F), most discriminatory between myeloid/erythroid ($p = 5.23 \times 10^{-65}$) and megakaryocyte/erythroid ($p = 1.97 \times 10^{-25}$) lineages. Progenitor-based *Blvrb* bivariate scatter plots demonstrated strongest positive correlation with the ERY cluster *Rhd* (Rh antigen), negative correlation with the MK cluster *Pf4* (platelet factor 4), and lack of correlation within the MY cluster *Mpo* (myeloperoxidase) (Fig. 2G). These computational models [1] contextually placed *Blvrb* at the intersection of ROS-generating and stress hematopoietic pathways, and [2] further imputed *Blvrb*-restricted lineage effects on erythroid/megakaryocyte partitioning independent of other heme degradation pathway genes.

Blvrb$^{-/-}$ mice display MK-biased stress thrombopoiesis.

Model validation was evaluated in *Blvrb*-null mice on a C57/BL6 background, using a targeting construct designed to delete *Blvrb* exons 2–4 [31] (Fig. 3A). F1 (heterozygote) crosses revealed genotypes of the expected Mendelian frequency (1:2:1 *Blvrb*$^{+/+}$:*Blvrb*$^{+/-}$:*Blvrb*$^{-/-}$), confirming the viability of *Blvrb*$^{-/-}$ mice with no gender imbalance. Immunoblot analysis and densitometric quantification of organs from *Blvrb*$^{-/-}$ mice confirmed Blvrb absence, and there were no reciprocal effects on heme degradation pathway proteins except for ~50% reduction of Hmox1 and Blvra in the spleen (Fig. 3B). Mutations within the BLVRB catalytic domain enhance MK ROS production in CD34^{+} hematopoietic cells [21]; however, *Blvrb*$^{-/-}$ platelets display normal thrombin (0.5 U/mL)-induced platelet P-selectin expression (Fig. 3C), excluding an acquired ROS-associated platelet defect. Similarly, UV–Vis spectrometry of erythrocytes from male and female *Blvrb*$^{-/-}$ mice demonstrated no evidence for metHb accumulation (Fig. 3D), indicating that *Blvrb* is not required for proper methemoglobin reduction during basal hematopoiesis. Our breeding program over 12-months demonstrated no hematological differences between gender- and age-matched *Blvrb*$^{+/+}$ or *Blvrb*$^{-/-}$ mice (Supplementary Fig. 1), and necropsies at 8-, 26- and 52-week time points demonstrated no pathology, results collectively establishing that *Blvrb* is dispensable for normal organ development and hematopoietic function during basal hematopoiesis.

We addressed predicted *Blvrb* functions in stress hematopoiesis by challenging mice with 5-fluorouracil (5-FU) to characterize hematopoietic lineage consequences in reconstitution and recovery [33,34]. There were no differences in hematopoietic recovery in young (2–4 month old) mice (Supplementary Fig. 2), and subsequent studies focused on mice >12 months of age to specifically assess age-restricted bias in HSC lineage speciation [3,35–37]. Pre-treatment and nadir (Day 7) blood cell counts were nearly identical between *Blvrb*$^{-/-}$ and *Blvrb*$^{+/+}$ cohorts, although *Blvrb*$^{-/-}$ mice demonstrated >2-fold exaggerated platelet counts at peak recovery (Day 14) compared to control ($p < 0.01$; N = 6/cohort) (Fig. 3E). Indeed, three of six *Blvrb*$^{-/-}$ mice platelet counts were >11×10^{6}/μL, whereas normal platelet counts for aged mice are ~1.8×10^{6}/μL [38]. Complete hematopoietic recovery in *Blvrb*$^{-/-}$ mice at Day 28 excluded long-term post-stress consequences on bone marrow function, and detailed necropsy and histological studies of other organs established a post-stress phenotype restricted to the hematopoietic compartment. There were no statistically significant

differences in red blood cell (RBC) nadir or leukocyte recovery at Day 14; production of newly generated reticulated platelets (RP) (peaking at Day 7) or erythroid reticulocytes (peaking at Day 14) were nearly identical between cohorts. The exaggerated rebound thrombocytosis in $Blvrb^{-/-}$ mice unaccompanied by increased RP% suggested that the thrombopoietic response was not due to enhanced proplatelet formation. Since platelet hyper-recovery is known to occur in 5-FU-treated mice by an unknown mechanism [39], we compared these results to an immune-mediated platelet recovery model that bypasses 5-FU effects on cycling hematopoietic progenitor cells [34] (Fig. 3F and G). Both $Blvrb^{+/+}$ and $Blvrb^{-/-}$ mice exhibited comparable platelet nadirs 24 h post-infusion with complete recovery to baseline by Day 8, and no statistically significant differences in RP generation; expectedly, there were no effects on erythroid counts or reticulocyte percentages in either cohort. These data collectively established that the $Blvrb^{-/-}$ stress thrombopoietic response resulted from effects on cycling progenitor cells.

In addition to a stress cytoprotective defect in $Blvrb^{-/-}$ hematopoietic organs (*vide infra*), bone marrow biopsies were most striking for megakaryocyte-biased expansion with no concomitant myeloid bias based on flow cytometric CD45$^+$-positivity ($Blvrb^{+/+}$, 34.0 ± 2.5% vs. $Blvrb^{-/-}$, 31.1 ± 2.4%, N = 3/cohort; not significant). Indeed, $Blvrb^{-/-}$ bone marrow biopsies revealed ~5-fold expansion of MKs compared to $Blvrb^{+/+}$ controls (Fig. 4A and B); many MKs appeared in clusters and expressed von Willebrand factor (vWF) as an enriched marker of MK-emergent stress hematopoiesis [6]. Previous data have established a requisite role for ROS production in MK differentiation [40], and the ROS^{high}CD41$^+$ subset from $Blvrb^{-/-}$ bone marrows post 5-FU treatment was ~3-fold greater than that of $Blvrb^{+/+}$ mice (Fig. 4C). These results contrasted with nearly identical ROS^{high}CD41$^+$ fractions by genotype during steady-state hematopoiesis; expansion of ROS^{high}CD41$^+$ subset from $Blvrb^{-/-}$ bone marrows post-stress were consistent with the differential MK quantification by bone marrow histology. Propidium iodide staining demonstrated no differences in cellular ploidy post-stress (Fig. 4D), most consistent with post-commitment megakaryocyte expansion with no concomitant effect on MK development [21].

Blvrb maintains a requisite cytoprotective function in hematopoietic stress recovery.

MK-biased stress recovery in $Blvrb^{-/-}$ mice occurred in conjunction with a hematopoietic repopulation defect involving both bone marrow and splenic tissues. $Blvrb^{-/-}$ bone marrow biopsies post 5-FU demonstrated relative hypocellularity (p <0.001, N > 8/cohort) and diminished cellular recovery in comparison to $Blvrb^{+/+}$ bone marrow biopsies (Fig. 5A–C). Prussian blue stains for bone marrow storage ferric (Fe^{3+}) iron were comparable, excluding defective iron utilization as a cause for hematopoietic (erythroid) loss. Naïve (untreated) $Blvrb^{-/-}$ bone marrow flushes displayed cellular recovery and histologically normal bone marrow biopsies comparable to $Blvrb^{+/+}$ mice, excluding chronic cellular damage and hematopoietic loss in the setting of $Blvrb$ deficiency. Whereas post-stress spleens of $Blvrb^{+/+}$ mice demonstrated cellular engorgement and splenomegaly, $Blvrb^{-/-}$ spleens revealed striking size diminution (p <0.001; N >8/cohort) with no concomitant effects on liver size (Fig. 5D and E; Supplementary Table 1). Splenic histology confirmed that defective hematopoietic reconstitution evident in $Blvrb^{-/-}$ mice was not caused by splenic fibrosis as previously described in aging (>12-month-old) $Hmox^{-/-}$ mice [41]. Instead, spleens

demonstrated selective loss of red pulp constituents (erythrocytes/macrophages) with general preservation of the lymphoid-predominant white pulp. Comparable expression of *CD163* (Type 1 cysteine-rich scavenger receptor) transcripts between *Blvrb*$^{-/-}$ and *Blvrb*$^{+/+}$ spleens (Fig. 5F) excluded selective loss of M2 macrophages, as previously described in *Hmox1*-deficient mice [41].

The *Blvrb*$^{-/-}$ splenic repopulation defect is comparable to that previously described in haploinsufficient *Hmox1*$^{+/-}$ mice [42], prompting more detailed studies of expression patterns of heme degradation proteins in liver and spleens post treatment with 5-FU. Expectedly, Blvrb was not present in organs from *Blvrb*$^{-/-}$ mice; Blvra and Hmox2 expression levels were nearly unchanged in both organs, and limited Hmox1 upregulation was restricted to livers of *Blvrb*$^{-/-}$ mice (Fig. 5G). The relatively stable patterns of protein expression during stress are comparable to those in unstimulated mice (refer to Fig. 3). Finally, Q-PCR of splenic antioxidant genes glutathione peroxidase (*Gpx 1*), superoxide dismutase (*Sod 1*, *Sod 2*, *Sod 3*), catalase (*Cat*) or the cellular antioxidant transcription factor (*Nrf 2*/*Nfe2l2*) were nearly identical between *Blvrb*$^{-/-}$ and *Blvrb*$^{+/+}$ cohorts (Supplementary Fig. 3), excluding a global defect in antioxidant handling in *Blvrb*$^{-/-}$ mice. These collective results establish that Blvrb has a requisite function in stress cytoprotection distinct from other well-characterized pathways, with predominant (if not exclusive) hematopoietic effects.

Blvrb$^{-/-}$ stress erythropoiesis displays defective lipid peroxidation.

Hematopoietic loss was associated with defective erythroid cytoprotection as established by probing peripheral blood erythrocytes for the presence of the lipid peroxidation product 4-hydroxynonenal (4-HNE) [43], a known marker of cellular oxidative stress or redox imbalance resulting from impaired intracellular bilirubin production [44]. Comparable and low-level HNE positivity was evident in steady-state erythrocytes from both *Blvrb*$^{+/+}$ and *Blvrb*$^{-/-}$ cohorts, presumably due to physiological senescence. In contrast, erythrocytes from stressed *Blvrb*$^{-/-}$ mice displayed a discrete ~28 kDa anti-HNE adduct evident at Day 7 (Fig. 6A and B), and the HNE-positive adduct persisted to Day 14, a time point corresponding to delayed splenic erythroid recovery in *Blvrb*$^{-/-}$ mice. Immunoreactive Blvra was detectable at stable levels in erythrocytes of both *Blvrb*$^{+/+}$ and *Blvrb*$^{-/-}$ cohorts (Fig. 6A), and there were no differences in Blvra activity between genotypes at baseline and post-5-FU stress (Fig. 6C). Lipid peroxidation was not associated with altered erythroid glutathione reductase or catalase activity (Fig. 6D), establishing non-redundancy from predominant erythroid antioxidant mechanisms. These data excluded reciprocal induction of a previously characterized BV IXα/BR IXα antioxidant cycle [12,44], and established a requisite Blvrb function in stress-induced erythroid cytoprotection, functioning independently of glutathione [44].

Consequences of defective lipid peroxidation on erythropoiesis were subsequently characterized by flow cytometry, designed to quantify successive stages of erythroid development using size and expression patterns of Ter119 (pan-erythroid marker, glycophorin A) and CD44 (erythrocyte hyaluronate receptor) [45]. Flow analysis using 7-aminoactinomycin (7-AAD) as a marker of cell viability confirmed expansion of non-viable

hematopoietic cells in 5-FU-stressed $Blvrb^{-/-}$ bone marrows, results consistent with the repopulation loss evident by histology (Fig. 5); no genotypic differences in 7-AAD viability were seen during basal hematopoiesis (Fig. 6E). Contraction of viable hematopoietic cells in 5FU-stressed $Blvrb^{-/-}$ mice was accompanied by relative expansion of the Ter119$^+$ subset (Fig. 6F and inset); there was no evidence for differential Ter119$^+$ partitioning between viable (7AAD$^-$) and non-viable (7AAD$^+$) subsets (Supplementary Fig. 4). Finally, erythroid development during basal and post-5-FU stress was largely comparable between $Blvrb^{+/+}$ and $Blvrb^{-/-}$ mice (Fig. 6F), excluding developmental block as a stage-restricted mechanism for erythropoietic damage.

The developmental bias and integrity of $Blvrb^{-/-}$ HSCs was subsequently characterized using methylcellulose multipotential progenitor (MPP) cultures, designed to delineate the proliferative and lineage-restricted potential of stressed HSCs *in vitro*. Day 14 MP P assays demonstrated nearly identical colony numbers between $Blvrb^{+/+}$ and $Blvrb^{-/-}$ mice (Fig. 6G), excluding a *Blvrb*-restricted effect on stem cell viability. In contrast, there was an ~1.7-fold expansion of multiprogenitor CFU-GEMMs (colony forming units, granulocytes/erythrocytes/monocytes/megakaryocytes) in bone marrows from $Blvrb^{-/-}$ mice compared to wild-type controls (68.2 ± 7.9 vs. 40.4 ± 4.6; $p = 0.004$); significant differences were not observed between naïve $Blvrb^{+/+}$ and $Blvrb^{-/-}$ mice (Supplementary Fig. 5).

Cell lineage distribution of CFU-GEMMs was established by Q-PCR using genetic markers specific for megakaryocytes, myeloid cells, and erythrocytes, along with *Blvra*, *Blvrb* and *Hmox1* (Fig. 6H). Expectedly, CFU-GEMMs derived from $Blvrb^{-/-}$ mice were deficient in *Blvrb*. We saw no inducible changes in *Blvra* or *Hmox1* between genotypes. In contrast, $Blvrb^{-/-}$ CFU-GEMMs demonstrated ~5-fold increased expression of megakaryocyte-specific *platelet factor 4* (*Pf4*) compared to $Blvrb^{+/+}$ colonies; *Pf4* up-regulation was accompanied by a reciprocal decrease of *Hbb* (erythroid) and *Ptprc* (CD45) genes. These results confirmed that the megakaryocyte-biased reprogramming potential of $Blvrb^{-/-}$ hematopoietic stem cells developed as an intrinsic cue unrelated to modulating effects from the stromal cell compartment [46].

3. Discussion

Using computational and *in vivo* validation studies, we identify Blvrb in a cytoprotective pathway of stress hematopoiesis, with divergent effects on post-commitment lineage fate. Previous RNASeq studies using purified human platelets identified *BLVRB* as a single thrombocytosis risk allele in cohorts with both clonal and non-clonal thrombocytosis, and redox-defective BLVRB displays MK-enhancing effects in CD34$^+$-hematopoietic stem cells *in vitro* [21]. We extended these initial observations using computational models to contextually place *Blvrb* function (s) in a stress hematopoietic pathway previously implicated in HSC survival and progenitor bias [29]. Interestingly, the NF-κB (nuclear factor-kappa B)-regulated TNF-α signaling response is postulated to be co-opted in aging HSCs, and a restricted phenotype in aged (>12 month) mice further positions Blvrb between distinct pathways regulating hematopoietic responses during stress [6] and aging [3,22]. While stress [6]- and age-related [3,35–37] progenitor lineage bias have been previously demonstrated, the $Blvrb^{-/-}$ stress hematopoietic phenotype has divergent effects on lineage

speciation, manifest by exaggerated thrombopoiesis occurring in the background of defective erythropoiesis. Comparable reciprocal bilineage phenotypes (progressive anemia with exaggerated platelet counts) were previously suggested in human thrombocytosis cohorts substratified by the presence of a redox-defective BLVRB mutation [21]. These observations validate the relevance of murine $Blvrb^{-/-}$ studies to humans.

The stress hematopoietic defect in $Blvrb^{-/-}$ mice, retaining an intact heme oxygenase system, defines Blvrb in a physiologically relevant and non-redundant mechanism of cytoprotection against cell stress [8]. Previous reports of the antioxidant activity of the biliverdin reductase system have attributed this activity to BLVRA and its role in the generation of the antioxidant bilirubin IXα [12,47,48]. However, loss of erythroid cytoprotection and the accumulation of an HNE modified protein in $Blvrb^{-/-}$ erythrocytes provides evidence for a role for Blvrb in maintaining cellular redox balance independently of the Hmox/Blvra system. This activity may be limited to erythrocytes, where Blvrb remains highly expressed under stress-induced conditions. Hematopoietic loss was evident in both bone marrows and spleens of 5FU-stressed $Blvrb$-deficient mice, although we saw limited direct effects on bone marrow erythroid development at the single Day 14 time point studied. Indeed, HSC depletion was accompanied by relative expansion of the erythroid Ter119$^+$ subset (with no clear partitioning between live and apoptotic erythroid fractions), most consistent with temporally-restricted effects on erythroid recovery. Murine 5FU stress cytotoxic recovery of recycling stem cells results in sequential megakaryocyte to erythroid repopulation [39], characterized by an initial wave of MK repopulation (typically at Days 6–8), followed by secondary erythroid repopulation (beyond Day 10). More detailed characterization of $Blvrb$-regulated erythroid recovery and development will require time-structured dynamic repopulation studies using single-cell transcriptomics to better delineate molecular events defining Blvrb-regulated mechanisms of erythroid cytoprotection and recovery.

Interestingly, the erythroid antioxidant defect is associated with HNE modification of a discrete protein with a molecular mass similar to that of an N-terminal cytoplasmic domain fragment of erythrocyte band 3 (CDB3) protein (the band is ~28 kDa and band 3 fragments are ~24 and 34 kDa) [49]. Band 3 has been proposed as a plausible mechanism for target membrane peroxidation and erythroid senescence by cooperative metHb binding to the cytoplasmic domain of oxidized band 3 [50]. Endogenous cleavage of CDB3 is likely due to caspase 3 [51] which is known to become activated due to oxidative stress in erythrocytes [52]. To our knowledge, HNE modification of CDB3 has not been reported, and experiments to identify the modified protein and/or acquired defects involving metHb accumulation during post-stress erythroid recovery remain ongoing.

$Blvrb^{-/-}$ mice phenocopy the hematopoietic defect(s) previously described in human [24] and murine [25] $Hmox1$ deficiency, further highlighting the critical role of an intact heme degradation pathway in basal and stress hematopoiesis. While heme proteins are found in the majority of eukaryotic cells and tissues, heme enrichment in erythroid cells (which contain ~80% of organismal heme) presumably accounts for the hematopoietic-restricted phenotype evident in murine models of heme degradation pathway deficiency [25,42,53]. While the rarity of the disease limits the phenotypic characterization of human $HMOX1$--associated

hematological defect(s), the better-characterized murine $Hmox1^{-/-}$ phenotype causes age-dependent anemia, defective iron utilization, and progressive splenic fibrosis [53]. Evidence for acquired and selective macrophage loss in murine $Hmox1^{-/-}$ deficiency is supported by the phenotypic rescue of the hematopoietic defect using macrophage-restricted bone marrow transplantation [41,54]. Based on splenic RNA analysis and tissue iron stains, we see no evidence for comparable macrophage defects in $Blvrb^{-/-}$ mice. In contrast to the phenotype of murine $Hmox1$ deficiency, haploinsufficient $Hmox1^{+/-}$ mice display a more restricted phenotype leading to a disrupted response to acute stress in stem cells and progenitors [55], with defective stress erythropoiesis in 5-FU-treated mice [42]. This stress phenotype is comparable to that described in $Blvrb^{-/-}$ mice, although effects on megakaryocytopoiesis were not characterized in $Hmox1^{+/-}$ mice [42]. Recently reported $Blvra^{-/-}$ mice demonstrate differences in plasma oxidation profiles manifest by increased ratios of cholesterol ester hydroperoxides to cholesteryl esters (CE-OOH:CE), and increased levels of α-tocopherol presumably due to impaired production of bilirubin IXα. $Blvra^{-/-}$ mice also displayed increased oxidative stress, as judged by defects in erythroid peroxiredoxin 2 activity [56]; however, effects on steady-state erythropoiesis appear minimal. The role(s) of $Blvra$ in stress hematopoiesis have not been described.

Stress-associated megakaryocytic hyperplasia and thrombocytosis were evident in the setting of defective erythroid repopulation, suggesting divergent effects of $Blvrb$-deficiency on lineage speciation. An immune-depleting thrombocytopenic model failed to recapitulate the exaggerated post-stress thrombocytotic response, most consistent with a Blvrb mechanism regulating megakaryocyte-biased stem cell speciation. Our initial stress model focused on 5FU to comprehensively define Blvrb-regulated effects on lineage recovery and development. Additional stressors may provide synergistic clues on stress hematopoiesis regulated by Blvrb, although lineage effects may be restricted by stressors such as TNF-α (which induces myeloid-biased regeneration) [29] or interferon-α (which induces stem-like megakaryocyte-committed progenitors) [5]. Hematopoietic stem cells are heterogeneous, and lineage speciation is regulated by intrinsic cues [37] and further modulated by complex cellular interactions encompassing the vascular niche [57,58]. A cell-autonomous effect on megakaryocytopoiesis is supported by MPP assays, which demonstrated expansion of CFU-GEMMs, coupled with lineage-exaggerated MK bias predicated on genetic markers. These results are consistent with those previously described using genetically-modified CD34+ HSCs expressing redox-defective BLVRB, which also showed colony-specific expansion of CFU-GEMMs and enhanced colony-forming units-megakaryocyte (CFU-MK) [21]. We saw no differences in aggregate colony formation between $Blvrb^{+/+}$ and $Blvrb^{-/-}$ MPP assays, precluding a cytotoxic effect on early progenitor cells.

The divergent results on erythropoiesis and megakaryocytopoiesis are most consistent with differential redox and cytoprotective mechanisms of lineage speciation occurring at discrete time points of hematopoietic development. Our computational models documented $Blvrb$ as a dominant erythroid transition gene in murine single-cell RNA hematopoietic studies [26,59], displaying coordinate expression with erythrocyte Rhd and reciprocal expression with megakaryocyte $Pf4$; there was no correlation with myeloid Mpo, strongly suggesting a partitioning effect restricted to erythroid/megakaryocyte lineage speciation. These studies complement our previous observation that, among heme degradation genes, only $Blvrb$

displayed temporally distinct expression patterns during megakaryocytopoiesis and erythropoiesis [21], peaking early during MK development, with late-onset and sustained induction during erythroid development. Indeed, BLVRB overexpression sufficiently promotes erythroid colony formation in CD34^{+}-hematopoietic stem cells *in vitro*, and redox-defective BLVRB (Ser111Leu) leads to ROS accumulation as the putative signal for MK-enhancing effects [21]. These studies also revealed that CD34^{+}-hematopoietic stem cells infected with lentivirus/BLVRB[Ser111Leu] result in a statistically significant increase of CD41^{+} CFU-MKs, in comparison to cells infected with wild type BLVRB [21]. Since BLVRB binds non-productively to other tetrapyrroles such as protohemin [18] or BV IXα [60], redox activity and cellular commitment could be modulated by endogenous cellular heme byproducts with resultant effects on redox coupling, cytoprotection, and lineage speciation [58]. Previous data have established that p22[hox]-dependent NADPH oxidase activity is responsible for ROS production and required for megakaryocyte differentiation [40], and these collective data suggest that the temporally-restricted nature of BLVRB redox activity provides the developmentally-regulated signal for exaggerated post-commitment megakaryocytopoiesis from bifurcating megakaryocyte/erythroid progenitor (MEP) cells during hematopoietic stress; an additive ROS-enhancing effect on proplatelet formation during late-stage megakaryocyte development cannot be excluded [61].

Rate-limiting release of biliverdin IXα from heme-bound HMOX is accelerated by BLVRA [62], although cooperative HMOX/BLVRB interactions have not been defined. Human BLVRB crystal structure demonstrates no evidence for dimerization [60], and a compulsory ordered kinetic mechanism has been proposed in which NADPH binding followed by substrate (e.g. BV) results in the sequential release of product (e.g. BR) and oxidized cofactor [17,63,64]. Predicated on x-ray crystallography [60] and thermodynamic modeling [65], we previously identified BLVRB inhibitors displaying inhibitory constants (K_i) in the low micro-molar [17,66]. Crystallography confirmed binding within the ligand-binding pocket [66], demonstrating critical interactions involving residue(s) immediately contiguous to the critical Ser[111], which was identified as the redox-defective mutant predisposing to thrombocytosis [21]. These inhibitors cause loss of redox coupling *in vitro*, and may now be used to address target validity and further refine lineage-restricted mechanisms of BLVRB inhibition during basal and stress hematopoiesis.

4. Methods

Computational model development and analysis.

Hematopoietic single cell transcriptomic raw sequencing data were obtained from GEO (accession number GSE81682), and included 1,920 hematopoietic stem and progenitor cells (HSPC) derived from 12-week-old female mice. All analyses were performed in the R programming environment (https://www.r-project.org), and pre-processing, clustering and marker identification were performed using the SEURAT package [67]. Our filtering (pre-processing) step excluded 264 cells expressing (*i*) less than 4,000 detected genes, (*ii*) less than 200,000 reads mapped to nuclear genes, or (*iii*) more than 10% of mapped reads mapping to the mitochondrial genome. After removing unwanted cells, we normalized the data for each cell using total expression, scaled by a factor of 10^4, and followed by $\log_{10}$-

transformation. Genes exhibiting high variability across cells were identified using the variance-stabilizing method, and 2,000 genes with the highest standardized variance were used as input of principle components analysis (PCA), using the first 30 principle components for downstream analyses. Clustering was performed using a KNN (K-Nearest Neighbors) graph based on the Euclidean distance in the PCA space, and edge weights between any two cells were assigned by the Jaccard similarity followed by the Louvain algorithm to cluster cells. The resulting 1,656 cells were divided into nine clusters using a resolution of 0.7 for cluster separation, and marker genes were determined by comparing gene expression between cells in the cluster and all remaining cells. Genes expressed in at least 25% of cells in either of the two groups and whose $\log_2$ (fold-change) was at least 0.25 between the two groups were tested for differential expression using the Wilcoxon rank sum test with the Benjamini-Hochberg multiple-test correction. For each cluster, markers were ranked by $\log_2$ (fold-change), and used in pre-ranked GSEA applying curated C2 and Hallmark 2 gene sets in the Molecular Signature Database (MSigDB, version 7.0) as references [30]. Gene sets that had overlaps with ranked markers of the size 15 to 100 were selected to run pre-ranked GSEA on 1,000 permutations (fgsea package). The Pearson correlation coefficient was applied to quantify relationships between two genes within individual clusters, expanded to encompass combined megakaryocyte/erythroid clusters given lineage development from common progenitors [23]; the permutation test was applied to test the null hypothesis that the true correlation coefficient was 0.

Factor analysis.

A Gaussian noise model was used for factorial single-cell latent variable model (f-scLVM); f-scLVM was applied to decompose single-cell transcriptome heterogeneity into interpretable biological drivers [27], using Hallmark gene sets derived from MSigDB version 7.0 [30]. Factor analysis was performed using Slalom [27]; false positive rate (FPR) and false negative rate (FNR) for assigning genes to factors are 0.01 and 0.001, respectively; mad_filter was set to 0.2. For fitting, five hidden factors were expected to be included, and gene sets with at least 15 genes presented in the single-cell transcriptomic dataset were retained. To exclude outliers, factors with mean absolute deviation lower than 0.2 were filtered out.

Generation and characterization of *Blvrb*$^{−/−}$ mice.

Mice were housed at the Stony Brook University Division of Laboratory Animal Resources where they were provided with water and food *ad libitum.* Targeted deletion of murine *Blvrb* exons 2–4 was completed in C57/BL6 embryonal stem cells using *Flp*/FRT for site-specific homologous recombination of the LacZ replacement cassette [31], followed by generation of chimeric mice as previously described [68]. Chimeric mice mated with C57/BL6 mice for eight generations were used to ensure germline transmission, and two distinct F1 (heterozygous) crosses served as the foundation for tracking patterns of Mendelian inheritance and gender; genotypes were confirmed using tail snips and genotyping primers are available upon request. *In vivo* studies were gender-matched and restricted to mice >12 months to assess age-restricted bias in HSC lineage speciation [3,35–37], coupled with the previously described age-dependent hematopoietic phenotype of *Hmox1*$^{−/−}$ mice [41,53].

For terminal experiments, mice were euthanized by CO_2 inhalation, followed by cervical dislocation.

Murine phenotypic and histologic studies.

Freshly isolated mouse organs were immediately snap-frozen in liquid nitrogen (for RNA or protein isolation), or paraffin embedded in 10% neutral buffered formalin for 16 h at 4 °C prior to histological stains using hematoxylin and eosin (H&E), Masson's Trichrome (collagen fibers), or Gomori Prussian Blue (determination of ferric iron accumulation) [69]. Immunohistochemical detection of megakaryocyte von Willebrand factor (vWF) was completed in deparaffinized sections using rabbit polyclonal vWF primary antibody (1:5000; Proteintech, Rosemont, IL) followed by peroxidase-based signal detection using anti-rabbit peroxidase-labeled polymer and liquid DAB (3,3′-Diaminobenzidine) plus chromogen (EnVision 2-component system, Agilent, Santa Clara, CA). All microscopic analyses were performed blinded to genotype.

Blood isolated by submandibular puncture served as the source for automated complete blood counts (CBCs) on a veterinary multi-species Hemavet 950 hematology analyzer (Drew Scientific, Miami Lakes, FL). Platelet activation assays were completed using freshly-prepared gel-filtered platelets isolated from individual mice as previously described [70], and cell-surface P-selectin was quantified by flow cytometry using Alexa Fluor 647-conjugated anti-mouse CD62P (1:10 dilution; BD Biosciences, Franklin Lakes, NJ).

Cytopenia induction experiments.

The chemotherapeutic agent 5-fluorouracil (5-FU) (Fresenius Kabi, USA) was diluted to 50 mg mL^{-1} with sterile saline, and age-matched $Blvrb^{-/-}$ and $Blvrb^{+/+}$ mice were injected with a single intraperitoneal dose of 5-FU at a final concentration of 150 mg kg^{-1} on Day 0. CBCs were measured at 24 h before 5-FU injection (Day –1) to determine baseline cell counts, and weekly until experimental completion. Mouse weights and phenotypic observations were recorded at baseline, and every two to three days until the experiment was terminated. Immune platelet depletion was completed using a single intraperitoneal dose of 1.5 μL g^{-1} of rabbit anti-thrombocyte serum (Accurate Chemical & Scientific Corporation, Westbury NY), followed by post-injection CBCs at Day 1 and Day 8.

Flow cytometry.

Bone marrow cells were isolated from dissected femurs using a previously described centrifugation method [71]. Hematopoietic cell-surface immunophenotyping of total bone marrow cells was completed as previously described [32], by incubating cells on ice for 15 min in the dark with lineage-restricted monoclonal antibodies (MAb) (BD Biosciences; Franklin Lakes, NJ): FITC (fluorescein isothiocyanate)-conjugated anti-CD41 [integrin αIIb, megakaryocyte] and PE (phycoerythrin)-conjugated anti-CD45 [myeloid cells] or APC (allophycocyanin)-conjugated anti-CD44 [hyaluronate receptor, erythrocyte] and FITC-conjugated anti-TER-119 [Glycophorin A, erythrocyte]. 7-AAD (7-amino-actinomycin D) (Biolegend, San Diego, CA) was used for dead cell exclusion. Intracellular ROS accumulation was quantified using the cell-permeant fluorogenic probe CellROX Red [500 nM, 30 min at 37 °C] (Life Technologies; Carlsbad, CA), followed by FITC-conjugated anti-

CD41 for dual detection of ROS/CD41. Flow cytometric quantification was completed by data acquisition of 10,000 events using logarithmic gain settings for light scatter and fluorescence detection, applying isotype-matched IgG controls for gate delineation (BD Accuri C6 Flow Cytometer); data were analyzed using Kaluza Flow Cytometry Analysis Software. A previously established gating method was employed to identify stage-specific erythroblast development using size and expression characteristics of erythroid markers TER-119 and CD44 [45].

To assess cellular DNA content, cells were fixed in 70% ethanol overnight at 4 °C, washed with DPBS (Dulbecco's phosphate buffered saline), and incubated in 500 µl Propidium Iodide (PI)/RNAse Staining Buffer (BD Pharmingen; San Jose, CA) for 15 min at room temperature for flow cytometric ploidy determinations [71].

Quantification of reticulated platelets (RP) and reticulocytes was completed on whole blood using thiazole orange (TO) (Sigma-Aldrich; St. Louis, MO). A 1 mg mL^{-1} stock solution of TO (in methanol) was diluted 1:20,000 in phosphate-buffered saline (PBS) containing 2 mM EDTA and 0.2% sodium azide. Whole blood (5 µL) was added to 1 mL of dilute TO dye and samples were incubated at room temperature in the dark for 30 min for flow cytometric quantification of nucleic acid-containing platelet and erythrocyte subpopulations.

Molecular analyses.

Expression levels of individual mRNAs were quantified using fluorescence-based real-time quantitative PCR (Q-PCR) technology, all as previously described [72]. Oligonucleotide primer pairs were generated using Primer 3 software (version 0.4.0, http://bioinfo.ut.ee/primer3–0.4.0), validated *in silico* and tested for optimal performance with SYBR green. All primers were designed to amplify specific cDNAs and give PCR products ranging in size from 199 to 201 bp. Each pair of primers passed two steps of *in-silico* validation – (*i*) using Genome Browser at UCSC for perfect match and (*ii*) using Primer Design and Search Tool at Bisearch for potential non-specific amplification. In addition, PCR performance was optimized using gradient PCR. Relative mRNA abundance was determined from triplicate assays performed in parallel using the comparative threshold cycle number (-Ct method), using actin mRNA was used as normalization control. Oligonucleotide primers sequences are provided in Supplementary Table 2.

Hematopoietic assays.

Multipotential progenitor colony assays were completed in methylcellulose cultures using MethoCult GF M3434 (STEMCell Technologies, Vancouver, Canada). Hematopoietic progenitors were plated in triplicate (2×10^4 cells/plate) and morphologically enumerated blinded to genotype at Day 12 post-plating [21]. Colonies were individually extracted from cultures for subsequent RNA isolation using Trizol [72].

Immunoblotting analysis.

Tissues were lysed by sonication in cold RIPA buffer (Rockland Immunochemical; Pottstown, PA) containing protease inhibitor cocktail (Millipore Sigma cat#P8340) and phosphatase inhibitor cocktail (Millipore Sigma cat#524625) using alternating 15-s on/30-

sec off bursts for 1 min at 50% amplitude. Cellular debris was removed by centrifugation at 10,000×*g* for 15 min at 4 °C, and protein concentrations were determined by use of the bicinchoninic acid (BCA) assay [73] with bovine serum albumin (BSA) as standard. Protein lysates were size-fractionated by SDS-PAGE [21], and immunodetection was completed using sheep anti-Blvrb antibody (1:1,000; R&D Systems; Minneapolis, MN cat#AF6568) followed by donkey anti-sheep antibody (1:10,000; Jackson ImmunoResearch; West Grove, PA; cat#713–035-147); mouse anti-actin antibody (1:1,000; Thermo Fisher Scientific; Waltham, MA cat#MA1–744) followed by sheep anti-mouse antibody (1:10,000; GE Healthcare; Chicago, IL cat#NA9310); rabbit anti-Blvra (1:1,000; Enzo Life Sciences; Farmingdale, NY cat#ADI-OSA-450-E) followed by goat anti-rabbit antibody (1:10,000; Enzo Life Sciences, cat#ADI-SAB-300-J); mouse anti-heme oxygenase I (1:1000; Novus Biologicals; Centennial, CO cat#NBP1–97507) followed by sheep anti-mouse antibody (1:10,000); mouse anti-heme oxygenase 2 (1:100; Santa Cruz; Dallas, TX cat#sc-17786) followed by sheep anti-mouse antibody (1:10,000); or mouse anti-HNE antibody (1:1,000; Thermo Fisher Scientific, cat#MA5–27570) followed by sheep anti-mouse antibody (1:10,000 dilution). Immunodetection was completed by enhanced chemiluminescence using Luminata™ Forte Western HRP substrate and visualized using a LI-COR C-DiGit® blot scanner. ImageJ software [74] was used for all densitometry calculations. Each band was measured three times applying the coefficient of variation to minimize error and average values were used for normalization.

Biochemical activity assays.

Erythrocyte lysis was achieved in buffer (1X PBS containing protease and phosphatase inhibitor cocktail on ice for 15 min, and cytoplasmic lysates were isolated from cellular debris after centrifugation at 10,000×*g* for 15 min at 4 °C. Human embryonic kidney 293 cells (HEK 293) lysates were prepared in lysis buffer by sonication (on ice) in 10-s bursts with 1-min cooling at an amplitude of 50%. Blvra assays were performed in the scanning kinetics mode (800–400 nm) using a Cary 60 UV/Vis spectrophotometer and enzymatic activity was monitored following the conversion of biliverdin IXα (ε_{650nm} = 14.3 mM^{-1} cm^{-1}) to bilirubin IXα (ε_{450nm} = 53 mM^{-1} cm^{-1}) [14]. Reactions were run in 100 mM CHES (pH 8.7) containing 100 μM NADPH and 20 μM biliverdin IXα (MilliporeSigma; St. Louis, MO) at 37 °C and were initiated by the addition of 200 μg of erythrocyte lysate or 100 μg of HEK 293 lysate as positive control; reactions without lysates (buffer control) displayed no activity. Catalase activity was monitored using 2 μg of erythrocyte lysates, quantifying decomposition of hydrogen peroxide at 240 nm (http://www.worthington-biochem.com/CTL/) using a Cary 60 UV/Vis spectrophotometer. The reaction mixture containing 50 mM potassium phosphate, pH 7.0 and 30% hydrogen peroxide (prepared in 50 mM potassium phosphate, pH 7.0) was pre-incubated at 25 °C for 3 min prior to addition of erythrocyte lysates, and reaction rates were determined from the linear portion of the curve. The ratio of reduced and oxidized glutathione was determined using freshly isolated erythrocytes and a luminescence-based system to detect and quantify total glutathione and GSH (reduced)/GSSG (oxidized) ratios (GSH/GSSG-Glo™ Assay; Promega; Madison, WI).

Statistics.

Statistical comparisons were completed using ANOVA or Student's t tests (or their non-parametric counterparts if the normality assumptions were not met) at the significance level of $p < 0.05$.

Study approval.

All murine studies were approved by the Stony Brook University IACUC (Institutional Animal Care and Use Committee), and judicious guidelines were followed to minimize mouse utilization and to ensure humane animal care.

Supplementary Material

Refer to Web version on PubMed Central for supplementary material.

Acknowledgments

References

[1]. Owusu-Ansah E, Banerjee U, Reactive oxygen species prime Drosophila haematopoietic progenitors for differentiation, Nature 461 (7263) (2009) 537–541. [PubMed: 19727075]

[2]. Oburoglu L, Tardito S, Fritz V, de Barros SC, Merida P, Craveiro M, et al., Glucose and glutamine metabolism regulate human hematopoietic stem cell lineage specification, Cell stem cell 15 (2) (2014) 169–184. [PubMed: 24953180]

[3]. Grover A, Sanjuan-Pla A, Thongjuea S, Carrelha J, Giustacchini A, Gambardella A, et al., Single-cell RNA sequencing reveals molecular and functional platelet bias of aged haematopoietic stem cells, Nat. Commun. 7 (2016) 11075. [PubMed: 27009448]

[4]. Pinho S, Marchand T, Yang E, Wei Q, Nerlov C, Frenette PS, Lineage-biased hematopoietic stem cells are regulated by distinct niches, Dev. Cell 44 (5) (2018) 634–641 e4. [PubMed: 29456137]

[5]. Notta F, Zandi S, Takayama N, Dobson S, Gan OI, Wilson G, et al., Distinct routes of lineage development reshape the human blood hierarchy across ontogeny, Science 351 (6269) (2016) aab2116. [PubMed: 26541609]

[6]. Haas S, Hansson J, Klimmeck D, Loeffler D, Velten L, Uckelmann H, et al., Inflammation-induced emergency megakaryopoiesis driven by hematopoietic stem cell-like megakaryocyte progenitors, Cell stem cell 17 (4) (2015) 422–434. [PubMed: 26299573]

[7]. Frezza C, Zheng L, Folger O, Rajagopalan KN, MacKenzie ED, Jerby L, et al., Haem oxygenase is synthetically lethal with the tumour suppressor fumarate hydratase, Nature 477 (7363) (2011) 225–228. [PubMed: 21849978]

[8]. Li Z, Nesbitt NM, Malone LE, Gnatenko DV, Wu S, Wang D, et al., Heme degradation enzyme biliverdin IXbeta reductase is required for stem cell glutamine metabolism, Biochem. J. 475 (6) (2018) 1211–1223. [PubMed: 29500232]

[9]. Abraham NG, Kappas A, Pharmacological and clinical aspects of heme oxygenase, Pharmacol. Rev. 60 (1) (2008) 79–127. [PubMed: 18323402]

[10]. Frankenberg-Dinkel N, Bacterial heme oxygenases, Antioxidants Redox Signal. 6 (5) (2004) 825–834.

[11]. Tenhunen R, Marver HS, Schmid R, Microsomal heme oxygenase characterization of the enzyme, J. Biol. Chem. 244 (23) (1969) 6388–6394. [PubMed: 4390967]

[12]. Baranano DE, Rao M, Ferris CD, Snyder SH, Biliverdin reductase: a major physiologic cytoprotectant, Proc. Natl. Acad. Sci. U. S. A 99 (25) (2002) 16093–16098. [PubMed: 12456881]

[13]. Stocker R, Yamamoto Y, McDonagh AF, Glazer AN, Ames BN, Bilirubin is an antioxidant of possible physiological importance, Science 235 (4792) (1987) 1043–1046. [PubMed: 3029864]

[14]. Yamaguchi T, Komoda Y, Nakajima H, Biliverdin-IX alpha reductase and biliverdin-IX beta reductase from human liver. Purification and characterization, J. Biol. Chem. 269 (39) (1994) 24343–24348. [PubMed: 7929092]

[15]. Cunningham O, Dunne A, Sabido P, Lightner D, Mantle TJ, Studies on the specificity of the tetrapyrrole substrate for human biliverdin-IXalpha reductase and biliverdin-IXbeta reductase. Structure-activity relationships define models for both active sites, J. Biol. Chem. 275 (25) (2000) 19009–19017. [PubMed: 10858451]

[16]. Franklin EM, Browne S, Horan AM, Inomata K, Hammam MA, Kinoshita H, et al., The use of synthetic linear tetrapyrroles to probe the verdin sites of human biliverdin-IXalpha reductase and human biliverdin-IXbeta reductase, FEBS J. 276 (16) (2009) 4405–4413. [PubMed: 19614742]

[17]. Zhang B, Nesbitt NM, Pereira PJB, Bahou WF, Biochemical characterization of biliverdins IXbeta/delta generated by a selective heme oxygenase, Biochem. J. 477 (3) (2020) 601–614. [PubMed: 31913441]

[18]. Xu F, Quandt KS, Hultquist DE, Characterization of NADPH-dependent methemoglobin reductase as a heme-binding protein present in erythrocytes and liver, Proc. Natl. Acad. Sci. U. S. A 89 (6) (1992) 2130–2134. [PubMed: 1549573]

[19]. Kutty RK, Maines MD, Purification and characterization of biliverdin reductase from rat liver, J. Biol. Chem. 256 (8) (1981) 3956–3962. [PubMed: 7217067]

[20]. McDonagh AF, Turning green to gold, Nat. Struct. Mol. Biol. 8 (3) (2001) 198–200.

[21]. Wu S, Li Z, Gnatenko DV, Zhang B, Zhao L, Malone LE, et al., BLVRB redox mutation defines heme degradation in a metabolic pathway of enhanced thrombopoiesis in humans, Blood 128 (5) (2016) 699–709. [PubMed: 27207795]

[22]. Carrelha J, Meng Y, Kettyle LM, Luis TC, Norfo R, Alcolea V, et al., Hierarchically related lineage-restricted fates of multipotent haematopoietic stem cells, Nature 554 (7690) (2018) 106–111. [PubMed: 29298288]

[23]. Debili N, Coulombel L, Croisille L, Katz A, Guichard J, Breton-Gorius J, et al., Characterization of a bipotent erythro-megakaryocytic progenitor in human bone marrow, Blood 88 (4) (1996) 1284–1296. [PubMed: 8695846]

[24]. Yachie A, Niida Y, Wada T, Igarashi N, Kaneda H, Toma T, et al., Oxidative stress causes enhanced endothelial cell injury in human heme oxygenase-1 deficiency, J. Clin. Invest. 103 (1) (1999) 129–135. [PubMed: 9884342]

[25]. Poss KD, Tonegawa S, Reduced stress defense in heme oxygenase 1-deficient cells, Proc. Natl. Acad. Sci. U. S. A 94 (20) (1997) 10925–10930. [PubMed: 9380736]

[26]. Nestorowa S, Hamey FK, Pijuan Sala B, Diamanti E, Shepherd M, Laurenti E, et al., A single-cell resolution map of mouse hematopoietic stem and progenitor cell differentiation, Blood 128 (8) (2016) e20–31. [PubMed: 27365425]

[27]. Buettner F, Pratanwanich N, McCarthy DJ, Marioni JC, Stegle O, f-scLVM: scalable and versatile factor analysis for single-cell RNA-seq, Genome Biol. 18 (1) (2017) 212. [PubMed: 29115968]

[28]. Subramanian A, Tamayo P, Mootha VK, Mukherjee S, Ebert BL, Gillette MA, et al., Gene set enrichment analysis: a knowledge-based approach for interpreting genome-wide expression profiles, Proc. Natl. Acad. Sci. U. S. A 102 (43) (2005) 15545–15550. [PubMed: 16199517]

[29]. Yamashita M, Passegue E, TNF-alpha coordinates hematopoietic stem cell survival and myeloid regeneration, Cell stem cell 25 (3) (2019) 357–372 e7. [PubMed: 31230859]

[30]. Liberzon A, Subramanian A, Pinchback R, Thorvaldsdottir H, Tamayo P, Mesirov JP, Molecular signatures database (MSigDB) 3.0, Bioinformatics 27 (12) (2011) 1739–1740. [PubMed: 21546393]

[31]. Skarnes WC, Rosen B, West AP, Koutsourakis M, Bushell W, Iyer V, et al., A conditional knockout resource for the genome-wide study of mouse gene function, Nature 474 (7351) (2011) 337–342. [PubMed: 21677750]

[32]. Zijlstra WG, Buursma A, Meeuwsen-van der Roest WP, Absorption spectra of human fetal and adult oxyhemoglobin, de-oxyhemoglobin, carboxyhemoglobin, and methemoglobin, Clin. Chem. 37 (9) (1991) 1633–1638. [PubMed: 1716537]

[33]. Radley JM, Scurfield G, Effects of 5-fluorouracil on mouse bone marrow, Br. J. Haematol. 43 (3) (1979) 341–351. [PubMed: 497116]

[34]. Schoedel KB, Morcos MNF, Zerjatke T, Roeder I, Grinenko T, Voehringer D, et al., The bulk of the hematopoietic stem cell population is dispensable for murine steady-state and stress hematopoiesis, Blood 128 (19) (2016) 2285–2296. [PubMed: 27357698]

[35]. Gekas C, Graf T, CD41 expression marks myeloid-biased adult hematopoietic stem cells and increases with age, Blood 121 (22) (2013) 4463–4472. [PubMed: 23564910]

[36]. Verovskaya E, Broekhuis MJ, Zwart E, Ritsema M, van Os R, de Haan G, et al., Heterogeneity of young and aged murine hematopoietic stem cells revealed by quantitative clonal analysis using cellular barcoding, Blood 122 (4) (2013) 523–532. [PubMed: 23719303]

[37]. Sanjuan-Pla A, Macaulay IC, Jensen CT, Woll PS, Luis TC, Mead A, et al., Platelet-biased stem cells reside at the apex of the haematopoietic stem-cell hierarchy, Nature 502 (7470) (2013) 232–236. [PubMed: 23934107]

[38]. Dayal S, Wilson KM, Motto DG, Miller FJ Jr., Chauhan AK, Lentz SR, Hydrogen peroxide promotes aging-related platelet hyperactivation and thrombosis, Circulation 127 (12) (2013) 1308–1316. [PubMed: 23426106]

[39]. Chenaille PJ, Steward SA, Ashmun RA, Jackson CW, Prolonged thrombocytosis in mice after 5-fluorouracil results from failure to down-regulate megakaryocyte concentration. An experimental model that dissociates regulation of megakaryocyte size and DNA content from megakaryocyte concentration, Blood 76 (3) (1990) 508–515. [PubMed: 2378983]

[40]. Sardina JL, Lopez-Ruano G, Sanchez-Abarca LI, Perez-Simon JA, Gaztelumendi A, Trigueros C, et al., p22phox-dependent NADPH oxidase activity is required for megakaryocytic differentiation, Cell Death Differ. 17 (12) (2010) 1842–1854. [PubMed: 20523355]

[41]. Kovtunovych G, Eckhaus MA, Ghosh MC, Ollivierre-Wilson H, Rouault TA, Dysfunction of the heme recycling system in heme oxygenase 1-deficient mice: effects on macrophage viability and tissue iron distribution, Blood 116 (26) (2010) 6054–6062. [PubMed: 20844238]

[42]. Cao YA, Kusy S, Luong R, Wong RJ, Stevenson DK, Contag CH, Heme oxygenase-1 deletion affects stress erythropoiesis, PloS One 6 (5) (2011), e20634. [PubMed: 21655188]

[43]. Castro JP, Jung T, Grune T, Siems W, 4-Hydroxynonenal (HNE) modified proteins in metabolic diseases, Free Radic. Biol. Med. 111 (2017) 309–315. [PubMed: 27815191]

[44]. Sedlak TW, Saleh M, Higginson DS, Paul BD, Juluri KR, Snyder SH, Bilirubin and glutathione have complementary antioxidant and cytoprotective roles, Proc. Natl. Acad. Sci. U. S. A 106 (13) (2009) 5171–5176. [PubMed: 19286972]

[45]. Chen K, Liu J, Heck S, Chasis JA, An X, Mohandas N, Resolving the distinct stages in erythroid differentiation based on dynamic changes in membrane protein expression during erythropoiesis, Proc. Natl. Acad. Sci. U. S. A. 106 (41) (2009) 17413–17418. [PubMed: 19805084]

[46]. Tikhonova AN, Dolgalev I, Hu H, Sivaraj KK, Hoxha E, Cuesta-Dominguez A, et al., The bone marrow microenvironment at single-cell resolution, Nature 569 (7755) (2019) 222–228. [PubMed: 30971824]

[47]. Sedlak TW, Snyder SH, Bilirubin benefits: cellular protection by a biliverdin reductase antioxidant cycle, Pediatrics 113 (6) (2004) 1776–1782. [PubMed: 15173506]

[48]. Liu Y, Liu J, Tetzlaff W, Paty DW, Cynader MS, Biliverdin reductase, a major physiologic cytoprotectant, suppresses experimental autoimmune encephalomyelitis, Free Radic. Biol. Med. 40 (6) (2006) 960–967. [PubMed: 16540391]

[49]. Rinalducci S, Ferru E, Blasi B, Turrini F, Zolla L, Oxidative stress and caspase-mediated fragmentation of cytoplasmic domain of erythrocyte band 3 during blood storage, Blood Transfus 10 (Suppl 2) (2012) s55–62. [PubMed: 22890269]

[50]. Arashiki N, Kimata N, Manno S, Mohandas N, Takakuwa Y, Membrane peroxidation and methemoglobin formation are both necessary for band 3 clustering: mechanistic insights into human erythrocyte senescence, Biochemistry 52 (34) (2013) 5760–5769. [PubMed: 23889086]

[51]. Mandal D, Moitra PK, Saha S, Basu J, Caspase 3 regulates phosphatidylserine externalization and phagocytosis of oxidatively stressed erythrocytes, FEBS Lett. 513 (2–3) (2002) 184–188. [PubMed: 11904147]

[52]. Mandal D, Baudin-Creuza V, Bhattacharyya A, Pathak S, Delaunay J, Kundu M, et al., Caspase 3-mediated proteolysis of the N-terminal cytoplasmic domain of the human erythroid anion exchanger 1 (band 3), J. Biol. Chem. 278 (52) (2003) 52551–52558. [PubMed: 14570914]

[53]. Poss KD, Tonegawa S, Heme oxygenase 1 is required for mammalian iron reutilization, Proc. Natl. Acad. Sci. U. S. A 94 (20) (1997) 10919–10924. [PubMed: 9380735]

[54]. Kovtunovych G, Ghosh MC, Ollivierre W, Weitzel RP, Eckhaus MA, Tisdale JF, et al., Wild-type macrophages reverse disease in heme oxygenase 1-deficient mice, Blood 124 (9) (2014) 1522–1530. [PubMed: 24963040]

[55]. Cao YA, Wagers AJ, Karsunky H, Zhao H, Reeves R, Wong RJ, et al., Heme oxygenase-1 deficiency leads to disrupted response to acute stress in stem cells and progenitors, Blood 112 (12) (2008) 4494–4502. [PubMed: 18509090]

[56]. Chen W, Maghzal GJ, Ayer A, Suarna C, Dunn LL, Stocker R, Absence of the biliverdin reductase-a gene is associated with increased endogenous oxidative stress, Free Radic. Biol. Med. 115 (2018) 156–165. [PubMed: 29195835]

[57]. Wang K, Zhang T, Dong Q, Nice EC, Huang C, Wei Y, Redox homeostasis: the linchpin in stem cell self-renewal and differentiation, Cell Death Dis. 4 (2013) e537. [PubMed: 23492768]

[58]. Suda T, Takubo K, Semenza GL, Metabolic regulation of hematopoietic stem cells in the hypoxic niche, Cell stem cell 9 (4) (2011) 298–310. [PubMed: 21982230]

[59]. Chen H, Albergante L, Hsu JY, Lareau CA, Lo Bosco G, Guan J, et al., Single-cell trajectories reconstruction, exploration and mapping of omics data with STREAM, Nat. Commun. 10 (1) (2019) 1903.

[60]. Pereira PJ, Macedo-Ribeiro S, Parraga A, Perez-Luque R, Cunningham O, Darcy K, et al., Structure of human biliverdin IXbeta reductase, an early fetal bilirubin IXbeta producing enzyme, Nat. Struct. Biol. 8 (3) (2001) 215–220. [PubMed: 11224564]

[61]. O'Brien JJ, Spinelli SL, Tober J, Blumberg N, Francis CW, Taubman MB, et al., 15-deoxy-delta12,14-PGJ2 enhances platelet production from megakaryocytes, Blood 112 (10) (2008) 4051–4060. [PubMed: 18755987]

[62]. Liu Y, Ortiz de Montellano PR, Reaction intermediates and single turnover rate constants for the oxidation of heme by human heme oxygenase-1, J. Biol. Chem. 275 (8) (2000) 5297–5307. [PubMed: 10681502]

[63]. Cunningham O, Gore MG, Mantle TJ, Initial-rate kinetics of the flavin reductase reaction catalysed by human biliverdin-IXbeta reductase (BVR-B), Biochem. J. 345 Pt 2 (2000) 393–399. [PubMed: 10620517]

[64]. Smith LJ, Browne S, Mulholland AJ, Mantle TJ, Computational and experimental studies on the catalytic mechanism of biliverdin-IXβ reductase, Biochem. J. 411 (2008) 475–484. [PubMed: 18241201]

[65]. Chu WT, Nesbitt NM, Gnatenko DV, Li Z, Zhang B, Seeliger MA, et al., Enzymatic activity and thermodynamic stability of biliverdin IXbeta reductase are maintained by an active site serine, Chemistry 23 (8) (2017) 1891–1900. [PubMed: 27897348]

[66]. Nesbitt NM, Zheng X, Li Z, Manso JA, Yen WY, Malone LE, et al., In silico and crystallographic studies identify key structural features of biliverdin IXbeta reductase inhibitors having nanomolar potency, J. Biol. Chem. 293 (15) (2018) 5431–5446. [PubMed: 29487133]

[67]. Stuart T, Butler A, Hoffman P, Hafemeister C, Papalexi E, Mauck WM 3rd, et al., Comprehensive integration of single-cell data, Cell 177 (7) (2019) 1888–1902 e21. [PubMed: 31178118]

[68]. Schmidt VA, Chiariello CS, Capilla E, Miller F, Bahou WF, Development of hepatocellular carcinoma in Iqgap2-deficient mice is IQGAP1 dependent, Mol. Cell Biol. 28 (5) (2008) 1489–1502. [PubMed: 18180285]

[69]. Sheehan DC, Hrapchak BB, Theory and Practice of Histotechnology, Mosby, St. Louis, 1980.

[70]. Bahou WF, Scudder L, Rubenstein D, Jesty J, A shear-restricted pathway of platelet procoagulant activity is regulated by IQGAP1, J. Biol. Chem. 279 (21) (2004) 22571–22577. [PubMed: 15026422]

[71]. Gertz JM, Meuser M, Bouchard BA, Simultaneous flow cytometric analysis of megakaryocyte polyploidy and a labile intracellular protein using zinc-based fixation, Cytometry Part A : the journal of the International Society for Analytical Cytology 91 (7) (2017) 713–720. [PubMed: 28692777]

[72]. Gnatenko DV, Dunn JJ, McCorkle SR, Weissmann D, Perrotta PL, Bahou WF, Transcript profiling of human platelets using microarray and serial analysis of gene expression, Blood 101 (6) (2003) 2285–2293. [PubMed: 12433680]

[73]. Smith PK, Krohn RI, Hermanson GT, Mallia AK, Gartner FH, Provenzano MD, et al., Measurement of protein using bicinchoninic acid, Anal. Biochem. 150 (1) (1985) 76–85. [PubMed: 3843705]

[74]. Schneider CA, Rasband WS, Eliceiri KW, NIH Image to ImageJ: 25 years of image analysis, Nat. Methods 9 (2012) 671–675. [PubMed: 22930834]
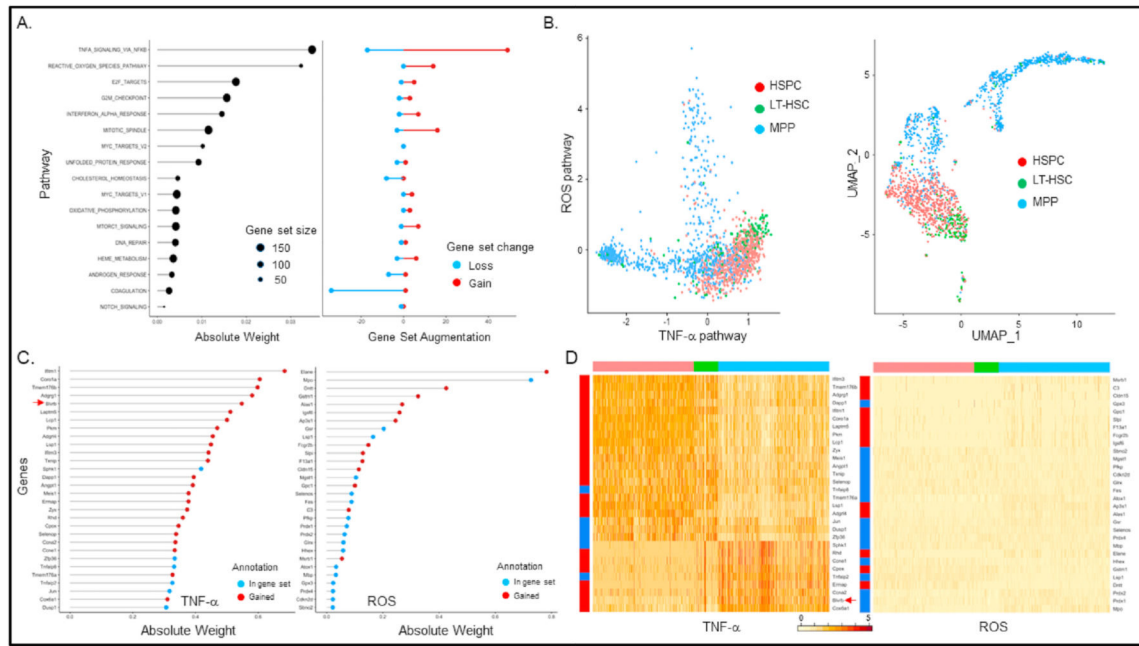
**Fig. 1. Pathway prediction models regulating hematopoietic development.**

A. Factor (pathway) relevance and gene set size of top annotated pathways identified using single cell latent variability model (f-scLVM) (*left panel*); gene set augmentation corresponding to top annotated pathways is shown (*right panel*). **B.** Bivariate visualization of cells using TNF-α (N = 228) and ROS (N = 60) pathway genes (*left panel*), or spatially reconstructed dimension reduction UMAP (uniform manifold approximation and projection) plots using the broader subset of highly variable genes (N = 2,000; *right panel*). Both plots were constructed using 1,656 cells delineated by hematopoietic phenotype. *LT-HSC* -Long-term hematopoietic stem cells; *HSPC* - hematopoietic stem progenitor cells; *MPP* - multipotential progenitor cells. **C.** Gene-modified weights for the most important genes (N = 30) in TNF-α (*left panel*) or ROS (*right panel*) pathways, delineating pre-annotated (*blue*) and model-added genes (*red*); *Blvrb* is delineated. **D.** Differential expression patterns using the 30-member TNF-α (*left panel*) or ROS (*right panel*) pathway genetic subsets demonstrating clustering by phenotype; for heat diagrams in both panels, columns correspond to color-coded HSC phenotypes (*Panel B*) and rows correspond to genes pre-annotated (*blue*) or added (*red*) by the sparse factor analytical model. Note that gene expression patterns added by the model correlate with those of pre-annotated genes (validating the factor identification model); relatively low-level expression of ROS pathway genes during steady-state hematopoiesis is evident. *Blvrb* is delineated by red arrow. (For interpretation of the references to color in this figure legend, the reader is referred to the Web version of this article.)
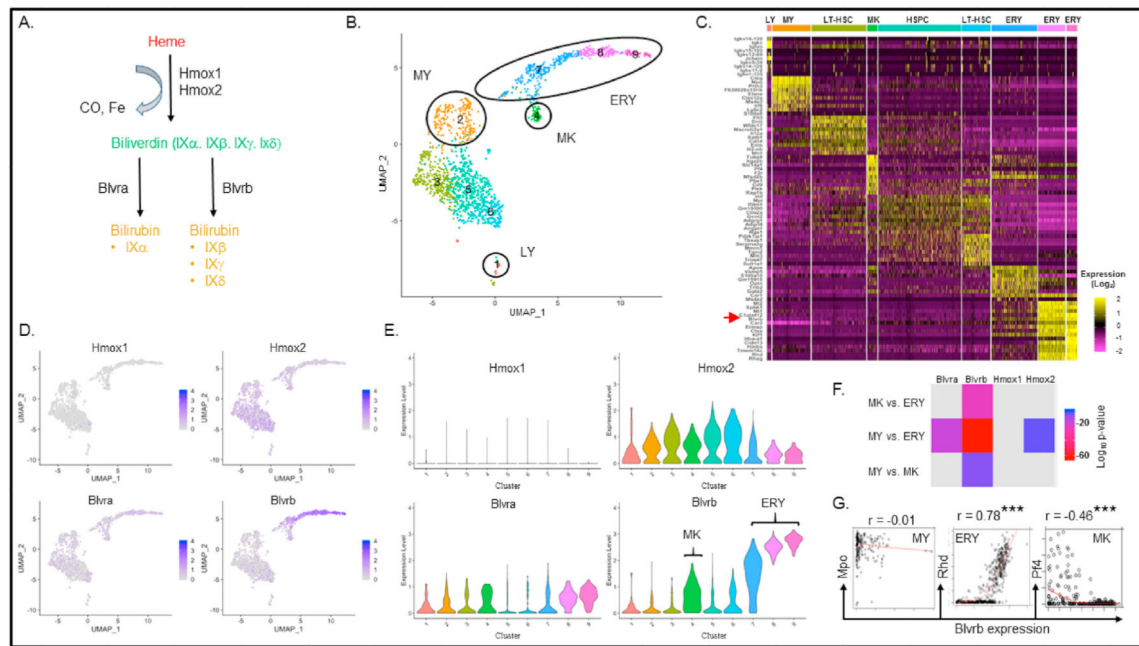
Fig. 2. *Blvrb* **lineage partitioning in hematopoiesis.**

<u>**A.**</u> Heme degradation schema showing divergent pathways delineated by isomeric biliverdins and reductases. <u>**B, C.**</u> Spatial reconstruction map of cell populations (*Panel B*) and genetically-annotated clusters displaying top 10 genes/cluster by lineage as defined by GSEA (*Panel C*; see Supplementary Table 1). LY – Lymphoid progenitors; MY – Myeloid progenitors; MK – Megakaryocyte progenitors; ERY – erythroid progenitors; *Blvrb* is highlighted (red arrow). <u>**D.**</u> Spatial reconstruction maps delineating heme degradation gene expression patterns (scale bar ($\log_2$ expression) is shown). <u>**E.**</u> Violin plots showing heme degradation gene expression patterns by cluster designation (lineages are color-coded as in *Panels B, C*). <u>**F.**</u> Heatmap showing adjusted p-values of heme pathway differentially-expressed genes between lineages (MK – megakaryocyte; MY – myeloid; ERY – erythroid); scale bar ($\log_{10}$ adjusted p-value). <u>**G.**</u> Lineage-specific *Blvrb* bivariate scatter plots were generated using highly-expressed lineage genes (myeloid *Mpo* (myeloperoxidase); erythrocyte *Rhd* (Rh antigen); megakaryocyte *Pf4* (platelet factor 4). The Pearson correlation coefficient (r) with fitted lines are shown in individual plots; ***p $\leq$ 0.001. (For interpretation of the references to color in this figure legend, the reader is referred to the Web version of this article.)
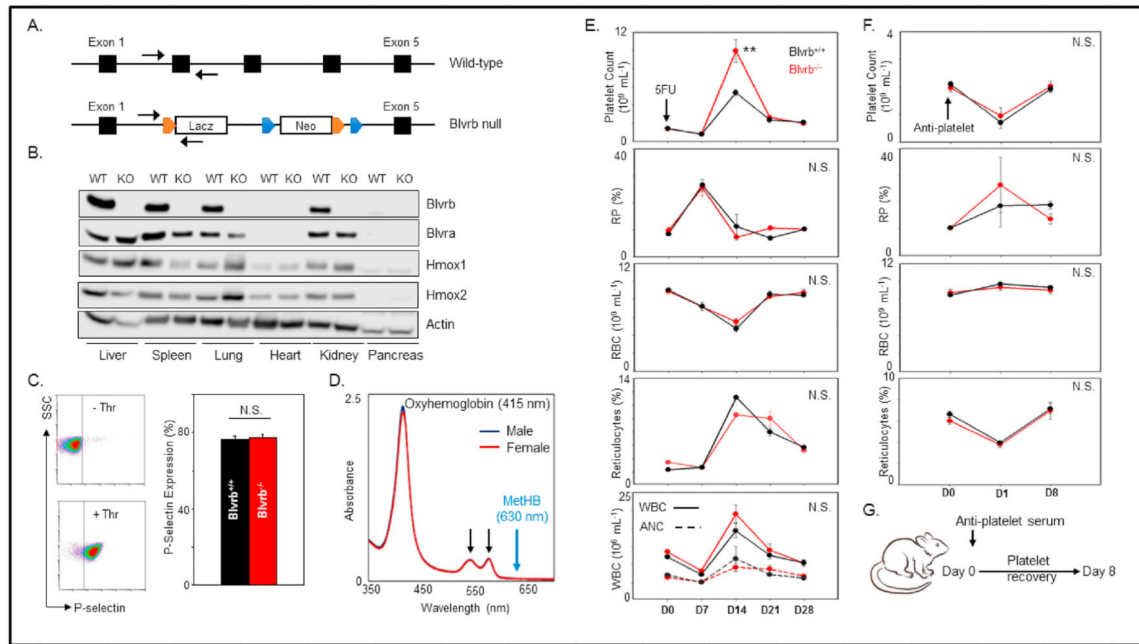
Fig. 3. Platelet-biased stress hematopoietic phenotype in *Blvrb*$^{-/-}$ mice.
A. Exon structure of wild-type allele (*top*) and targeted null allele (*bottom*). Location of flanking flippase recognition target (*FRT*, orange) used for site-directed recombination, *loxP* sites (blue) flanking Neo^R gene, and genotyping primers used for delineating wild-type and *Blvrb*-null alleles are shown. **B.** Immunoblots (20 μg/lane) of target organs analyzed for heme degradation pathway proteins. KO indicates *Blvrb*$^{-/-}$ and WT indicates *Blvrb*$^{+/+}$. **C.** Gel-filtered platelets were stimulated (or not) with thrombin (Thr, 0.5 U/mL; 5 nM) for 5 min followed by flow cytometric quantification of cell-surface P-selectin (expressed as mean ± SEM; N = 2 mice/cohort). **D.** UV–Vis (ultraviolet–visible light) spectra of erythrocyte lysate from male and female *Blvrb*$^{-/-}$ mice; the Soret band (415 nm) and Q-bands at 540 and 575 nm (black arrows) indicative of oxyhemoglobin are shown (32); note absence of the methemoglobin peak at 630 nm (blue arrow). **E, F.** Hemograms of age- and gender-matched mice treated with 150 mg kg^{-1} 5-FU (*Panel E*), or 1.5 μL g^{-1} platelet-neutralizing immunoglobulin (*Panel F;* infusion schema is shown in *Panel G*); results expressed as mean ± SEM, N > 6/cohort. RP, reticulated platelets; RBC, red blood cells; WBC, white blood cells; ANC, absolute neutrophil count. **p 0.01; N.S. - not significant. (For interpretation of the references to color in this figure legend, the reader is referred to the Web version of this article.)
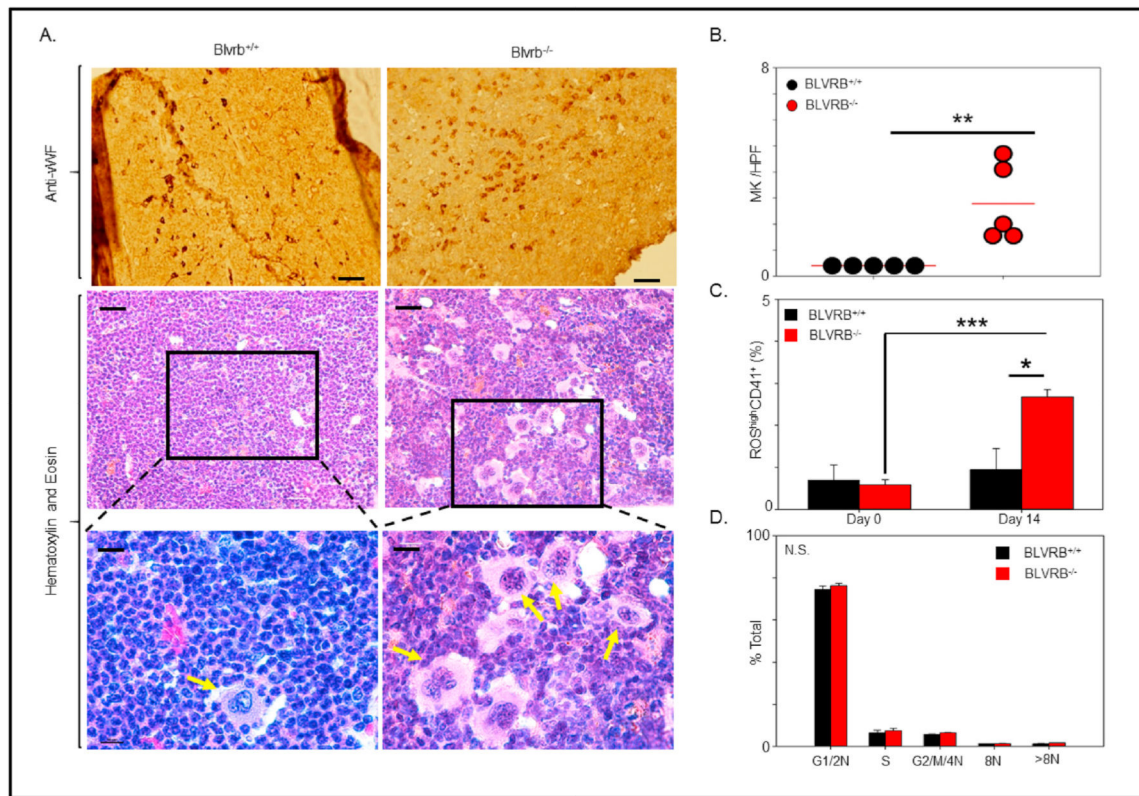
Fig. 4. Megakaryocyte-biased lineage expansion in hematopoietic stress.
A. Representative histology of Day 14 bone marrow biopsies stained with anti-vWF (*upper panel*) or hematoxylin and eosin (H&E, *middle* and *bottom panels*); megakaryocyte hyperplasia in *Blvrb*$^{-/-}$ mice is evident (yellow arrows); for all panels, size markers are shown. Scale bar-*upper panel* 100 μm, *middle panel* 25 μm, *bottom panel* 10 μm. **B.** Megakaryocyte quantification was completed blinded to genotype and expressed as MK/HPF (high-powered field, 1,000 X); data presented as mean ± SEM; MK quantification in unstimulated *Blvrb*$^{+/+}$ and *Blvrb*$^{-/-}$ mice is < 0.3 MK/HPF, *not shown*). **C.** Bone marrow cells were stained with CellRox green and PE-conjugated anti-CD41, and percent ROS^{high}/CD41$^+$ cells were quantified by flow cytometric analysis (data expressed as mean ± SEM, N = 3 mice/genotype). **D.** Ploidy analysis using propidium iodine staining of bone marrow cells (N = 3/genotype). (For interpretation of the references to color in this figure legend, the reader is referred to the Web version of this article.)
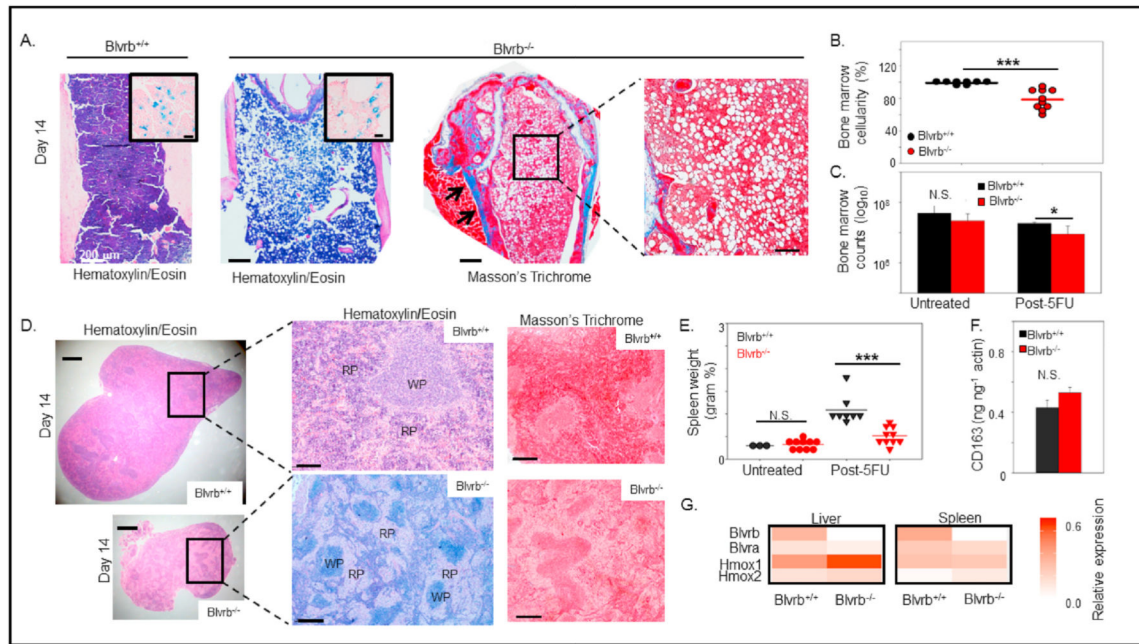
Fig. 5. Cytoprotective stress defect in *Blvrb*$^{-/-}$ mice is restricted to hematopoietic compartments. **A.** Representative histologic sections from bone marrow biopsies stained with hematoxylin and eosin (H & E), Masson's Trichrome, and Prussian blue (H & E insets) demonstrate relative hypocellularity in *Blvrb*$^{-/-}$ mice compared to *Blvrb*$^{+/+}$ littermate controls with normal storage iron (Fe^{+3}). Masson's trichrome confirms lack of collagen fibrosis in *Blvrb*$^{-/-}$ bone marrows (blue staining (arrows) reveals normal cortical collagen); for all sections, scale bars are shown. Scale bar- H&E 200 μm, *inset* 25 μm; Masson's Trichrome 200 μm **B.** Aggregated bone marrow cellularity data is presented as mean ± SEM; bone marrow cellularity in untreated *Blvrb*$^{+/+}$ and *Blvrb*$^{-/-}$ mice was 100% (data not shown). **C.** Bone marrow cellular counts obtained from femoral flushes in untreated and Day 14 post-5-FU mice (data expressed as mean ± SEM mL^{-1}, N = 3 mice/genotype). **D.** Splenic histological stains (H & E and Masson's Trichrome) completed on Day 14 post-5-FU shows clear size diminution in *Blvrb*$^{-/-}$ compared to *Blvrb*$^{+/+}$ spleens; note selective loss of red pulp (RP) constituents (erythrocytes/macrophages) with general preservation of the lymphoid-predominant white pulp (WP) in *Blvrb*$^{-/-}$ spleens with no evidence for collagen fibrosis (Masson's Trichrome stain); scale bars for all panels are shown. Scale bar-H&E 1 mm, *expanded view* 200 μm; Masson's Trichrome 200 μm **E.** Normalized splenic weights from untreated and 5-FU-treated mice (mean ± SEM). **F**. Q-PCR of haptoglobin receptor *CD163* mRNA transcripts in spleens from *Blvrb*$^{-/-}$ and *Blvrb*$^{+/+}$ mice. Data represent the mean ± SEM (N = 4 for *Blvrb*$^{-/-}$ and N = 3 for *Blvrb*$^{+/+}$) **G**. Densitometric quantification of heme degradation pathway proteins in hematopoietic organs (liver and spleen) normalized to actin. Scale bar (relative expression is shown). For all plots, *p   0.05; **p   0.01, ***p   0.001, N.S. - not significant. (For interpretation of the references to color in this figure legend, the reader is referred to the Web version of this article.)
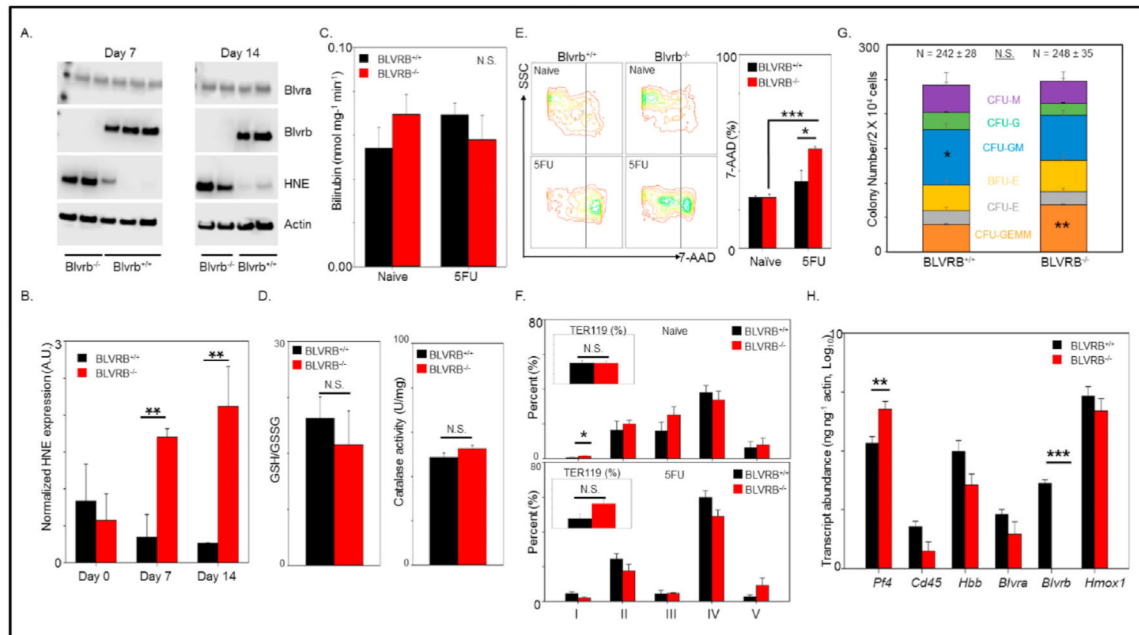
Fig. 6. Defective erythroid lipid peroxidation and lineage development in *Blvrb*^{−/−} mice.

A, B. Protein lysates (30 μg/lane) from *Blvrb*^{−/−} or *Blvrb*^{+/+} erythrocytes at Days 7 and 14 post-5-FU; densitometric quantification of the ~28 kDa adduct (α-HNE) normalized to actin is shown (*Panel B*, mean ± SEM, N = 2–4 mice/time point). **C.** Blvra activity in erythrocyte lysates in untreated (mean ± SEM; N = 4 for *Blvrb*^{−/−} and N = 6 for *Blvrb*^{+/+}) or Day 5-FU-stressed mice (N = 6 for *Blvrb*^{−/−} and N = 5 for *Blvrb*^{+/+}). **D.** Biochemical characterization of Day 14 post-5-FU stress erythrocyte antioxidant activity as a function of reduced to oxidized (GSH/GSSG) glutathione (mean ± SEM; N = 3 for *Blvrb*^{−/−} and N = 4 for *Blvrb*^{+/+}, *left panel*), or catalase activity (mean ± SEM; N = 4 for *Blvrb*^{−/−} and N = 5 for *Blvrb*^{+/+}, *right panel*). **E, F.** Representative flow cytometric scatter plots for detection of non-viable (7-AAD positive) hematopoietic fractions (*left panel*), or aggregated data (N = 3 mice/genotype (*right panel*). SSC – side scatter (cellular complexity). **F.** Bone marrow flow cytometry of erythroid developmental stage in steady-state (*Naive*) and Day 14-stressed mice. Erythroid development stages: I (proerythroblasts), II (basophilic), III (polychromatophilic), IV (orthochromatophilic), V (mature). Data are mean ± SEM (N = 3 mice/genotype); insets show total Ter119-positive (pan-erythroid) fractions. **G.** MPP assays using Day 14 bone marrow cells (2 × 10⁴ cells/plate), expressed as mean ± SEM, N = 9/genotype. *CFU-M*, colony forming units monocytes; *CFU-G*, colony forming units granulocytes; *CFU-GM*, colony forming units granulocytes and monocytes; *BFU-E*, burst forming units erythrocytes; *CFU-E*, colony forming units erythrocytes; *CFU-GEMM*, colony forming units granulocytes/erythrocytes/monocytes/megakaryocytes. **H.** Q-PCR of CFU-GEMM for lineage markers normalized to β-actin mRNA (mean ± SEM, N = >4/genotype). *Pf4*, platelet factor 4; *CD45*, protein tyrosine phosphatase receptor type C, *PTPRC*; *Hbb*, β-globin; *p 0.05; **p 0.01; ***p 0.001; N.S. – not significant.